

Unraveling the role of oxygen vacancy in the electrooxidation of 5-hydroxymethylfurfural on Co_3O_4

Yuxuan Lu

Hunan University

Tianyang Liu

Nanjing Normal University

Chunming Yang

Yan'an University

Chung-Li Dong

Tamkang University <https://orcid.org/0000-0002-4289-4677>

Yucheng Huang

Tamkang University

Yafei Li

Nanjing Normal University <https://orcid.org/0000-0002-6136-863X>

Bo Zhou

Hunan University

Ling Zhou

Hunan University

Yujie Wu

Hunan University

Zhijie Kong

Hunan University

Ming Yang

Hunan University

Yandong Wu

Hunan University

Weixing Zhao

Hunan University

Yuqin Zou (✉ yuqin_zou@hnu.edu.cn)

Hunan University

Shuangyin Wang

Hunan University <https://orcid.org/0000-0001-7185-9857>

Article

Keywords: 5-hydroxymethylfurfural, oxygen vacancy, electrocatalysts, spinel oxides, adsorption behavior

Posted Date: July 13th, 2021

DOI: <https://doi.org/10.21203/rs.3.rs-685285/v1>

License:   This work is licensed under a Creative Commons Attribution 4.0 International License.

[Read Full License](#)

Abstract

The electrooxidation of 5-hydroxymethylfurfural (HMF) offers a promising green route to attain high-value chemicals from biomass. The HMF electrooxidation reaction (HMFOR) is a complicated process involving the combined adsorption and coupling of organic molecules and OH^- on the electrode surface. An in-depth understanding of these cooperative adsorption behaviors and reaction processes is fundamentally essential. Herein, the adsorption behavior of HMF and OH^- , and the role of oxygen vacancy on Co_3O_4 are initially unraveled. Correspondingly, instead of the competitive adsorption of OH^- and HMF on the metal sites, it is observed that the OH^- could fill into oxygen vacancy (V_o) before couple with organic molecules through the lattice oxygen oxidation reaction process, which could accelerate the rate-determining step of the dehydrogenation of 5-hydroxymethyl-2-furancarboxylic acid (HMFCFA) and enhance the overall conversion of HMF on $\text{V}_\text{o}\text{-Co}_3\text{O}_4$. This work sheds a depth insight on the catalytic mechanism of oxygen vacancy, which benefits designing a novel strategy to modulate the multi-molecules combined adsorption behaviors.

Introduction

An increasing demand for energy and bulk chemicals to advance the growth and development of modern society will inevitably consume limited fossil resources such as coal, crude oil, and natural gas at an increasing rate.^{1,2} Moreover, increasing carbon emission and the resultant global warming have caused adverse changes to the climate, which has become global problems, in need of imperative solutions.³ A promising strategy includes the development of renewable and earth-rich biomass (e.g., lignocellulose, fat, and starch crops) as a substitute for fossil resources to develop a sustainable supply chain.^{4,5,6} 5-hydroxymethylfurfural (HMF) has been listed as the top 10 biomass-derived platform molecules by the U.S. Department of Energy, which can be oxidized to pharmaceutical intermediates, monomers, and agrochemicals.^{7,8,9} 2,5-furandicarboxylic acid (FDCA), as a typical product of the HMF conversion, is an essential monomer for the production of poly (ethylene 2,5-furandicarboxylate) to replace petroleum-based polyethylene terephthalate.^{10,11}

HMF electrocatalytic oxidation (HMFOR) is a promising approach to realize a high yield of FDCA at ambient temperature and pressure.^{12,13,14} The adsorption/desorption behavior is regarded as a critical step in the catalytic process.^{15,16,17} OH_{ad} is the crucial intermediate for the oxygen evolution reaction (OER) and alcohol molecules catalytic cycle, which has been widely recognized the reaction mechanism.^{18,19,20} In ethanol oxidation, the H^* derived from the dehydrogenation of hydroxyl groups is combined with OH_{ad} in the alkaline solution.^{20,21} Since the HMFOR process includes the oxidation of hydroxyl and aldehyde groups, different adsorption energies and sites of OH^- on catalysts significantly influence the HMFOR activity. Moreover, unlike OER, for which only OH^- adsorbed is involved, the competitive adsorption between OH^- and HMF molecules occurs on the limited reaction sites for HMFOR, leading to less efficient catalysis.²² Therefore, developing an effective strategy to address the adsorption

competition on catalysts at the atomic level is essential for the rational design of efficient electrocatalysts.

Constructing oxygen vacancies in spinel oxides is an efficient strategy for modulating the surface electronic structure and the intrinsic catalytic activity.²³ Therefore, it is essential to accurately identify the role of oxygen defects at the atomic level. Tremendous efforts have been made to elucidate and reveal the role of oxygen vacancies in various electrocatalytic reactions.^{24, 25, 26} However, for the electrocatalytic conversion of HMF, the environment of the electrolyte solution including both HMF molecules and OH⁻ is complicated. Thus, an in-depth understanding of the role of oxygen vacancy (Vo) in the process of HMFOR at the atomic level is important. Cobalt spinel oxides (Co₃O₄) have been extensively investigated for HMFOR due to abundant active site and tunable defect structure, which are considered as a type of ideal model catalysts.²⁷ Accordingly, Co₃O₄ is one of the representative platforms for directly investigating the adsorption behavior of OH⁻ and HMF molecules.

Herein, Co₃O₄ and Vo-Co₃O₄ were selected as catalysts to investigate the role of oxygen vacancies during the process of HMFOR. The structural evolution of Vo was characterized via operando XAS and quasi-operando XPS. Time-of-flight secondary ion mass spectrometry (TOF-SIMS) was conducted to trace the oxygen isotope-labeled OH⁻ during HMFOR. Combining experimental discoveries with DFT calculation, we found the nucleophilic OH⁻ tended to fill into Vo in the lattice of Vo-Co₃O₄ and further engaged the dehydrogenation and combination of HMF molecules via lattice OH, which could markedly accelerate the rate-determining step of the dehydrogenation of HMFCA and improve the catalytic activity of HMFOR on spinel oxides. This work sheds a depth insight on the catalytic mechanism of oxygen vacancy, which benefits designing a novel strategy to modulate the multi-molecules combined adsorption behaviors.

Results And Discussion

Co₃O₄ nanosheets were synthesized by an electrodeposition method, and the Vo was introduced by plasma treatment at Ar atmosphere (**Fig. 1a-b** and Supplementary Fig. 1-2).^{24, 28} The spinel structure of Vo-Co₃O₄ was identified by high-resolution transmission electron microscopy (HR-TEM) in Fig.1c, illustrating that the Vo-Co₃O₄ kept integral lattice structures after plasma treatment. The X-ray diffraction (XRD) patterns were clearly indexed to the spinel structure with *Fd-3m* space group for Vo-Co₃O₄ and Co₃O₄ (JCPDS No. 42-1467), and the extra peak marked by an orange diamond is attributed to Ti mesh (Fig. 1d). The existence of Vo in Co₃O₄ was further examined by O 1s XPS spectra, electron paramagnetic resonance (EPR) spectra, and extended X-ray absorption near-edge structure (EXAFS). A representative EPR signal at *g* = 2.002 was found in Vo-Co₃O₄, revealing the electron trapped by oxygen vacancies (Fig. 1e).^{29, 30} The surface Vo were derived from chemisorbed oxygen groups, which belonged to defect-oxide groups and the content of these Vo was further traced by O 1s spectra (Fig.1f).^{31, 32, 33} The relatively high content of Vo was found in the Vo-Co₃O₄ (78%). The EXAFS spectra were displayed in Fig. 1g. The first peak, which corresponded to the coordination shell, was the Co-O bond at ~ 1.5 Å.²⁴ The Co-O bond

intensity for $\text{Vo-Co}_3\text{O}_4$ was lower than that for Co_3O_4 , suggesting lower coordination between cobalt and oxygen.³⁴ The optimal fitting results of EXAFS spectra based on standard Co_3O_4 indicated that Co-O coordination of $\text{Vo-Co}_3\text{O}_4$ is unsaturated (Supplementary Table 1).

The electrochemical performance of $\text{Vo-Co}_3\text{O}_4$ and Co_3O_4 was evaluated by linear sweep voltammetry (LSV) measurement. The HMFOR activity was evaluated in 1 M KOH with 50 mM HMF in Fig. 1h, and a lower oxidation potential on $\text{Vo-Co}_3\text{O}_4$ than that of Co_3O_4 (1.44 V_{RHE}) was observed (1.37 V_{RHE} , the potential at 10 mA cm^{-2}), implying that Vo played a vital role in HMFOR process. The intrinsic activities of $\text{Vo-Co}_3\text{O}_4$ and Co_3O_4 were evaluated by normalizing the current with electrochemically active surface area (ECSA) and Brunauer-Emmett-Teller (BET) specific surface area (Supplementary Fig. S5). The electrochemical performance of $\text{Vo-Co}_3\text{O}_4$ was superior to Co_3O_4 under both conditions, showing that the existence of Vo enhanced the intrinsic activities of Co_3O_4 . The reaction rate was evaluated by Tafel slope in Supplementary Fig. S6, and the smaller Tafel slope for $\text{Vo-Co}_3\text{O}_4$ (117.5 mV dec^{-1}) than Co_3O_4 (122.6 mV dec^{-1}) suggested that Vo could accelerate reaction kinetics during HMFOR.

In the HMFOR process, the organic molecules and OH^- were adsorbed and combined on the electrode surface simultaneously (Fig. 1i).²⁰ Therefore, it is of great significance for catalysts to have the optimal OH^- and organic adsorption capability. The DFT calculation was conducted to confirm the vital role of Vo in HMFOR. The calculation results displayed the optimal adsorption model for the HMF molecule, which has two adsorption sites: the furan ring absorbed at the octahedral sites, the aldehyde/hydroxyl groups absorbed on the lateral tetrahedral sites, and the adsorption of OH^- located at lateral octahedral sites, as shown in **Fig. 2a**.³⁵ The reaction process was displayed in Fig. 2b, including the combination of HMF molecules with OH_{ad} to 5-hydroxymethyl-2-furancarboxylic acid (HMFCFA), the dehydrogenation of HMFCFA to formyl-2-furancarboxylic acid (FFCA), and the further combination of FFCA with OH_{ad} to FDCA. It was reported that the nucleophilic OH^- was filled into Vo and further directly contributed to O-O coupling in the process of OER.²⁶ In the HMFOR process, the calculation results revealed that the distance between OH_{ad} and reaction groups could be significantly reduced when the OH^- was filled into lateral Vo, which accelerated the process of combination of reactive molecules with lattice OH and improved reaction kinetics (the reaction process was displayed in Fig. 2d). Moreover, we have excluded the oxygen from aldehyde and hydroxyl groups filled into Vo (Supplementary Table 2) due to higher adsorption energies and unstable adsorption structures. Then the calculation of reaction state was used for investigating the specific reaction process in Fig. 2e. The reaction models were shown in Fig. 2e and Supplementary Fig. S7, identifying that the rate-determining step (RDS) is HMFCFA to FFCA in the HMFOR process. The lower reaction barriers in this step were discovered in $\text{Vo-Co}_3\text{O}_4$ (1.17 eV) than Co_3O_4 (1.67 eV), indicating that the OH^- filled into Vo favored the dehydrogenation of HMFCFA and improved RDS kinetics in the process of HMFOR.

To investigate OH^- adsorption behavior and establish the relationship between structure coordination and reaction process, the operando XANES, quasi-operando XPS, and TOF-SIMs were utilized to track the

change of $\text{Vo-Co}_3\text{O}_4$ and Co_3O_4 at the oxidation potential. No apparent change of Co K-edge and R-space was observed for $\text{Vo-Co}_3\text{O}_4$ in **Fig. 3a-b**, indicating the stable spinel structure of $\text{Vo-Co}_3\text{O}_4$ at different potentials, which is consistent with the results of XRD patterns and HR-TEM images (Supplementary Fig. 8-9). The valence of Co was evaluated by the shift of pre-edge in the Co K-edge and the fitted Co 2p orbit in the XPS spectra (Fig. 3c and Supplementary Fig. 10-11).²⁸ The results showed that the valence of Co on Co_3O_4 was nearly unchanged before HMFOR, suggesting that the OH⁻ adsorbed on the surface did not influence the coordination structure of Co, whereas, for $\text{Vo-Co}_3\text{O}_4$, the valence of Co increased before HMFOR (1.30 V_{RHE}) probably due to the saturated coordination by the filling of OH⁻ into Vo. When the potential is higher than the reaction potential (1.40 V_{RHE}), the increase of valence was detected for both $\text{Vo-Co}_3\text{O}_4$ and Co_3O_4 , which is due to the intrinsic oxidation of cobalt. The shift of pre-edge was used to evaluate the valence of Co at the 7720 eV (Fig. 3a inside), indicating that the trend of $\text{Vo-Co}_3\text{O}_4$ is similar to XPS results.^{24, 34, 36} In order to accurately detect the impact of Vo at oxidation potential, the coordination structure (CN) of $\text{Vo-Co}_3\text{O}_4$ was fitted according to the extended X-ray absorption near-edge structure (EXAFS).^{36, 37, 38} As shown in Fig. 3d and Supplementary Fig. S12, the CN number of Co-O bond increased at 1.30 V_{RHE} , suggesting that the OH⁻ was filled into Vo. Then the decreased coordination of Co-O found at 1.4-1.5 V_{RHE} indicates the consumption of lattice OH. The increase of CN number of Co-Co_{OH} suggests the structural evolution of Co_{Td} on $\text{Vo-Co}_3\text{O}_4$.

Moreover, the content of surface oxygen vacancies (Vo) was further traced by quasi-operando O 1s spectrum (Fig. 3e and Supplementary Figure 13).^{31, 32, 33} Compared with Co_3O_4 , the content of Vo decreased for $\text{Vo-Co}_3\text{O}_4$ as the potential increased, which could be attributed to the OH⁻ filled into Vo in the HMFOR process. Meanwhile, since the O¹⁸H⁻ could be derived from the hydrolysis and mixed with O¹⁶H⁻ in KOH, the isotope-labeling of H₂O¹⁸ was used for tracing the OH⁻ during HMFOR by TOF-SIMS in Fig. 3f.³⁹ The TOF-SIMS spectra of $\text{Vo-Co}_3\text{O}_4$ and Co_3O_4 electrode after HMFOR in 1 M KOH with 50 mM HMF in H₂O¹⁸ solution displayed a higher content of O¹⁸H⁻ for $\text{Vo-Co}_3\text{O}_4$ than Co_3O_4 , suggesting the filling of OH⁻ into lattice during HMFOR, and the traces amount of O¹⁸H⁻ in Co_3O_4 resulted from the intrinsic defect in Co_3O_4 . Compared with Co_3O_4 , the abundant OH in lattice could combine with HMF molecules and accelerate reaction kinetics.

Since the PBS solution has scarce OH⁻ which is only derived from water dissociation, the $\text{Vo-Co}_3\text{O}_4$ and Co_3O_4 were studied in the 1 M PBS with 50 mM HMF to evaluate the electrochemical activity in the deficient OH⁻ environment (Fig. 3g). The oxidation potential of $\text{Vo-Co}_3\text{O}_4$ (1.53 V_{RHE} , the potential at 10 mA cm⁻²) is lower than Co_3O_4 (1.65 V_{RHE}), indicating that the Vo had strong ability for the OH⁻ adsorption to reduce the reaction barrier of HMFOR.⁴⁰

To establish the structure-activity-potential relationship, the *in-situ* electrochemical impedance spectroscopy (EIS), an efficient technique for identifying the reaction interface, was employed (Fig. 4a-b and Supplementary Fig. 14).⁴¹ The high-frequency region (10¹ Hz-10⁵ Hz) is associated with the oxidation

of the electrode inner, and the oxidation of $\text{Vo-Co}_3\text{O}_4$ and Co_3O_4 electrodes occurred in this region.⁴² The low-frequency region (10^{-1} Hz- 10^1 Hz) is related to the nonhomogeneous charge distribution, namely the appearance of oxidation species at the electrode interface.¹⁰ In Fig. 4a and Supplementary Fig. 14, a peak found in the low-frequency region at the potential of $1.55 V_{\text{RHE}}$ suggested the OER occurred, which were also found when 50 mM HMF was added (Fig. 4b and Supplementary Fig. 14). However, an extra peak was observed at the potential of $1.30 V_{\text{RHE}}$ and $1.35 V_{\text{RHE}}$ for $\text{Vo-Co}_3\text{O}_4$ and Co_3O_4 , respectively, indicating the appearance of HMFOR. To further quantify the relationship between the oxidation of electrode inner and electrode interface reaction, the EIS data were fitted by the optimal fit model in Supplementary Fig. 15, and the fitting parameters were shown in Supplementary Table 3-6. The R_p and R_{ct} represented the resistance of the electrode inner oxidation and interface oxidation, respectively.^{21, 42, 43} For $\text{Vo-Co}_3\text{O}_4$, in Fig. 4c, the R_p dropped when the potential reached $1.1 V_{\text{RHE}}$, suggesting the structural evolution of catalysts. When the potential is higher than $1.3 V_{\text{RHE}}$, a decrease of the R_{ct} suggests the occurrence of oxidation reaction (HMFOR), which was posterior to oxidation of the electrode inner (Fig. 4d). This trend could also be observed on the Co_3O_4 electrode. For Co_3O_4 , a later dropping of R_p and R_{ct} than $\text{Vo-Co}_3\text{O}_4$ in Fig. 4c-d suggests a slower rate for inner oxidation and HMFOR process than $\text{Vo-Co}_3\text{O}_4$. The earlier oxidation of electrode inner for $\text{Vo-Co}_3\text{O}_4$ indicates the faster saturation of Co-O coordination by the filling of OH^- into Vo and thus contributes to the occurrence of HMFOR (Fig. 4e).

The co-existence of aldehyde and hydroxyl groups for HMF molecules could be oxidized to carboxylic acid and aldehyde; thus, there were two possible pathways for HMFOR (Fig. 5a).^{44, 45} Initially, the 2,5-diformylfuran (DFF) and HMFCa were originated from the oxidation of HMF molecules and were oxidized to FFCA. Subsequently, the final product of FDCA was obtained by oxidation of FFCA. The real-time monitoring of complicated intermediate and reaction processes is beneficial to identify the vital role of Vo in HMFOR. The concentration of substrates, intermediates, and products was quantified by periodically collecting the resultant electrolyte by potentiostatic electrolysis measurement at $1.47 V_{\text{RHE}}$. High-performance liquid chromatography (HPLC) was used to quantify standard substances and products (Supplementary Fig. 16). The concentration of intermediates and products was firstly evaluated in 1 M KOH with 10 mM HMF as shown in Fig. 5b and Supplementary Fig. 17. The concentration of HMFCa is the highest during the HMFOR process, showing that pathway I is dominated, and the sluggish kinetics step is HMFCa to FFCA at the strong alkaline solution, which is consistent with DFT results. However, the content of HMFCa for HMFOR on $\text{Vo-Co}_3\text{O}_4$ is lower than Co_3O_4 , indicating that the Vo could contribute to accelerating the reaction process of HMFCa to FFCA (Fig. 5c).²² Thus, the $\text{Vo-Co}_3\text{O}_4$ showed a higher yield (91.9%) and faradaic efficiency (88.1%) than Co_3O_4 (86.7% and 83.3%). Furthermore, the $\text{Vo-Co}_3\text{O}_4$ electrode also displayed a good stability for HMFOR (Supplementary Fig. S18).

The reaction process was investigated in the deficient OH^- environment (1 M PBS solution), as shown in Fig. 5d-e and Supplementary Fig. 19. The DFF concentration is higher than HMFCa, indicating that pathway II is governed in this process. Noticeably, the intermediate of DFF is found at 5-50 C for $\text{Vo-Co}_3\text{O}_4$ electrode, which dramatically reduces after 50 C with increasing the product FFCA and FDCA. On

the contrary, the stable concentration of DFF is detected until the HMF is consumed on the Co_3O_4 electrode, and the concentration of FDCA is constantly lower than that on $\text{Vo-Co}_3\text{O}_4$, indicating that Vo could accelerate the reaction process by faster catching OH^- and coupling with organic molecules in the process of HMFOR.

In summary, by combing various *in-situ* electrochemical characterizations with DFT studies, the role of Vo in the process of HMFOR on Co_3O_4 has been investigated in detail. Notably, instead of the competitive adsorption of OH^- and HMF on the active sites of Co_3O_4 , for $\text{Vo-Co}_3\text{O}_4$ catalysts, the Vo will adsorb OH^- from the electrolyte, which couple with organic molecules during HMFOR, evidenced by the saturation of Co-O coordination and increased valence of Co. The more straightforward coupling pattern could effectively reduce the reaction barrier of the rate-determining step and enhance the electrocatalytic performance of HMFOR. Therefore, the $\text{Vo-Co}_3\text{O}_4$ catalysts exhibit a higher reaction activity with a lower oxidizing potential ($1.37 \text{ V}_{\text{RHE}}$) than Co_3O_4 ($1.44 \text{ V}_{\text{RHE}}$). This work could provide a guideline for understanding the reaction mechanism of HMFOR and furthering the design of efficient and advanced electrocatalysts for HMFOR.

Methods

Synthesis. The pure Co_3O_4 nanosheet arrays were fabricated by the electrodeposition method in three-electrodes cell in a 0.05 M $\text{Co}(\text{NO}_3)_2$ aqueous electrolyte. In the electrodeposition process, working electrode and counter electrode is Ti mesh, and reference electrode is saturated calomel electrode (SCE). The electrodeposition potential is $-1.0 \text{ V}_{\text{SCE}}$. After 10 minutes electrodeposition, the green $\text{Co}(\text{OH})_2$ sample was obtain and then to be calcined at $250 \text{ }^\circ\text{C}$ for 2 hours with a heating rate of $1 \text{ }^\circ\text{C min}^{-1}$ to transform into Co_3O_4 . The $\text{Vo-Co}_3\text{O}_4$ nanosheets was synthesized via the treatment of Ar plasma at 250W and 100 Pa with 120 s.

Characterization. The TEM was performed on a Tecnai G2 F20. The XRD was conducted on Bruker D8 Advance diffractometer. The BET was measured by a Micromeritics ASAP 2020 V3.02 H. The XPS was taken using an SHIMADZU-KRATOS, AXIS SUPRA. The Raman was conducted on a Labram-010. The XANES was performed at TLS-BL17C at the National Synchrotron Radiation Research Center, Taiwan. The EPR was taken using a Bruker JES-FA200.

Electrochemical characterization. The LSV curves were performed with a CHI 760e electrochemical analyzer. The EIS was measured by autolab (PGSTAT302N). All the tests in the three-electrode cell unless noted otherwise, the catalyst was directly used as the working electrode, while the counter electrode and the reference electrode is graphite rod and SCE. LSV measurement was tested in an undivided cell and electrolysis test was measured in a divided cell with Nafion 117 membrane as the separator. Operando EIS measurement was conducted over a frequency range from 10^{-1} to 10^5 Hz with AC amplitude of 10 mV.

HPLC analysis. HPLC was measured by LC-2030C system with an ultraviolet-visible detector and Shim-pack GWS 5 μm C18 column. Specifically, sampling 50 μL of electrolyte and diluted to 1 mL ultrapure water and analyzing it by HPLC. The wavelength is set to 265 nm, mobile phase is methanol and 5 mM ammonium formate aqueous solution (3:7) with 0.6 ml min^{-1} .

The calculation of HMF conversion, FDCA yield and Faradaic efficiency using equations (1), (2) and (3), respectively.

$$\text{HMF conversion (\%)} = [n(\text{HMF consumed}) / n(\text{HMF initial})] \times 100 \quad (1)$$

$$\text{FDCA yield (\%)} = [n(\text{FDCA formed}) / n(\text{HMF initial})] \times 100 \quad (2)$$

$$\text{Faradaic efficiency (\%)} = [n(\text{FDCA formed}) / (\text{Charge} / (6 \times F))] \times 100 \quad (3)$$

where F is the Faraday constant (96485 C mol^{-1}) and n is the concentration of reactant.

Calculation Method. DFT computations were carried using plane-wave basis set in the Vienna ab initio Simulation Package (VASP).⁴⁶ The projector-augmented-wave (PAW) method was used for describing the ion-electron interaction.^{47, 48} All the DFT calculations were based on generalized gradient approximation (GGA) method with the Perdew-Burke-Ernzerhof (PBE) functional.⁴⁹ The electron localization state of Co-3d orbitals was corrected via DFT+U method, and the value of the effective Hubbard U term was set to 3.5 eV. The total energy and force convergence criteria were set as 1×10^{-4} eV and 0.1 eV/Å, respectively. We set the cut-off energy to be 420 eV and sampled the Brillouin zone with $3 \times 3 \times 1$ for geometry optimization. DFT-D3 (D stands for dispersion) procedure was adopted to describe van der Waals (vdW) interactions.⁵⁰ The climbing-image nudged elastic band (CI-NEB) method was used to obtain the energy barrier of reaction process.⁵¹

Declarations

Acknowledgements

This work was supported by the National Key R&D Program of China (2020YFA0710000), the National Natural Science Foundation of China (grant Nos. 21902047, 21825201, U19A2017), the Provincial Natural Science Foundation of Hunan (2016TP1009 and 2020JJ5045), and Changsha Municipal Natural Science Foundation (kq2007007). The synchrotron X-ray absorption spectroscopy (XAS) data were obtained at TLS-BL17C at the National Synchrotron Radiation Research Center (NSRRC).

Author contributions

Shuangyin Wang and Yuqin Zou conceived the idea and supervised the work. Yuxuan Lu performed most experiments and wrote the manuscript. Chunming Yang and Bo Zhou directed the research and analyzed and interpreted the data. Chung-Li Dong and Yucheng Huang performed in situ XAS and analyzed corresponding data. Zhijie Kong, Ling Zhou and Yujie Wu performed operando EIS and analyzed

corresponding data. Tianyang Liu and Yafei Li performed the DFT calculations. Weixing Zhao., Ming Yang and Yandong Wu performed the TEM characterization. All of the authors have read the manuscript and agree with its content.

Competing interests

The authors declare no conflict of interest.

Reference

1. Chu S, Majumdar A. Opportunities and challenges for a sustainable energy future. *Nature* **488**, 294-303 (2012).
2. Staffell I, *et al.* The role of hydrogen and fuel cells in the global energy system. *Energy Environ. Sci.* **12**, 463-491 (2019).
3. Chu S, Cui Y, Liu N. The path towards sustainable energy. *Nat. Mater.* **16**, 16-22 (2016).
4. Ennaert T, *et al.* Potential and challenges of zeolite chemistry in the catalytic conversion of biomass. *Chem. Soc. Rev.* **45**, 584-611 (2016).
5. Tang C, Zheng Y, Jaroniec M, Qiao SZ. Electrocatalytic refinery for sustainable production of fuels and chemicals. *Angew. Chem. Int. Ed.* **133**, 2-21 (2021).
6. Prabhu P, Wan Y, Lee J-M. Electrochemical Conversion of Biomass Derived Products into High-Value Chemicals. *Matter* **3**, 1162-1177 (2020).
7. van Putten RJ, van der Waal JC, de Jong E, Rasrendra CB, Heeres HJ, de Vries JG. Hydroxymethylfurfural, a versatile platform chemical made from renewable resources. *Chem. Rev.* **113**, 1499-1597 (2013).
8. Bozell JJ, Petersen GR. Technology development for the production of biobased products from biorefinery carbohydrates—the US Department of Energy’s “Top 10” revisited. *Green Chem.* **12**, 525-728 (2010).
9. Yang Y, Mu T. Electrochemical oxidation of biomass derived 5-hydroxymethylfurfural (HMF): pathway, mechanism, catalysts and coupling reactions. *Green Chem.*, DOI: 10.1039/d1031gc00914a (2021).
10. Lu Y, *et al.* Identifying the Geometric site dependence of spinel oxides for the Electrooxidation of 5-Hydroxymethylfurfural. *Angew. Chem. Int. Ed.* **59**, 19215-19221 (2020).
11. Rajendran S, *et al.* Programmed photodegradation of polymeric/oligomeric materials derived from renewable bioresources. *Angew. Chem. Int. Ed.* **54**, 1159-1163 (2015).

12. Zhang N, *et al.* Electrochemical oxidation of 5-Hydroxymethylfurfural on nickel nitride/carbon nanosheets: reaction pathway determined by in situ sum frequency generation vibrational spectroscopy. *Angew. Chem. Int. Ed.* **58**, 15895-15903 (2019).
13. You B, Jiang N, Liu X, Sun Y. Simultaneous H₂ generation and biomass upgrading in water by an efficient noble-metal-free bifunctional electrocatalyst. *Angew. Chem. Int. Ed.* **55**, 9913-9917 (2016).
14. You B, Liu X, Jiang N, Sun Y. A general strategy for decoupled hydrogen production from water splitting by integrating oxidative biomass valorization. *J. Am. Chem. Soc.* **138**, 13639-13646 (2016).
15. Jan Hulva, *et al.* Unraveling CO adsorption on model single-atom catalysts. *Science* **371**, 375-379 (2021).
16. Wu T, *et al.* Iron-facilitated dynamic active-site generation on spinel CoAl₂O₄ with self-termination of surface reconstruction for water oxidation. *Nat. Catal.* **2**, 763-772 (2019).
17. Yao Y, *et al.* Engineering the electronic structure of single atom Ru sites via compressive strain boosts acidic water oxidation electrocatalysis. *Nat. Catal.* **2**, 304-313 (2019).
18. Song J, *et al.* A review on fundamentals for designing oxygen evolution electrocatalysts. *Chem. Soc. Rev.* **49**, 2196-2214 (2020).
19. Tao HB, *et al.* A General Method to Probe Oxygen Evolution Intermediates at Operating Conditions. *Joule* **3**, 1498-1509 (2019).
20. Bender MT, Lam YC, Hammes-Schiffer S, Choi KS. Unraveling two pathways for electrochemical alcohol and aldehyde oxidation on NiOOH. *J. Am. Chem. Soc.* **142**, 21538-21547 (2020).
21. Chen W, *et al.* Activity origins and design principles of nickel-based catalysts for nucleophile electrooxidation. *Chem* **6**, 2974-2993 (2020).
22. Lu Y, *et al.* Tuning the selective adsorption site of biomass on Co₃O₄ by Ir single atoms for electrosynthesis. *Adv. Mater.* **33**, e2007056 (2021).
23. Xie C, *et al.* Defect chemistry in heterogeneous catalysis: recognition, understanding, and utilization. *ACS Catal.* **10**, 11082-11098 (2020).
24. Xiao Z, *et al.* Operando identification of the dynamic behavior of oxygen vacancy-rich Co₃O₄ for oxygen evolution reaction. *J. Am. Chem. Soc.* **142**, 12087-12095 (2020).
25. Yin J, *et al.* NiO/CoN Porous nanowires as efficient bifunctional catalysts for Zn-Air batteries. *ACS Nano* **11**, 2275-2283 (2017).

26. Huang Z-F, *et al.* Chemical and structural origin of lattice oxygen oxidation in Co–Zn oxyhydroxide oxygen evolution electrocatalysts. *Nat. Energy* **4**, 329-338 (2019).
27. Zhao Q, Yan Z, Chen C, Chen J. Spinels: Controlled preparation, oxygen reduction/evolution reaction application, and beyond. *Chem. Rev.* **117**, 10121-10211 (2017).
28. Xu L, *et al.* Plasma-engraved Co₃O₄ nanosheets with oxygen vacancies and high surface area for the oxygen evolution reaction. *Angew. Chem. Int. Ed.* **55**, 5277-5281 (2016).
29. Zhang K, Zhang G, Qu J, Liu H. Disorder the atomic structure of Co(II) oxide via B-Doping: an efficient oxygen vacancy introduction approach for high oxygen evolution reaction electrocatalysts. *Small* **14**, e1802760 (2018).
30. Zheng J, *et al.* Defect-enhanced charge separation and transfer within protection layer/semiconductor structure of photoanodes. *Adv. Mater.* **30**, e1801773 (2018).
31. Hu W, *et al.* Electron-pinned defect-dipoles for high-performance colossal permittivity materials. *Nat. Mater.* **12**, 821-826 (2013).
32. Hu H, Guan B, Xia B, Lou XW. Designed formation of Co₃O₄/NiCo₂O₄ double-shelled nanocages with enhanced pseudocapacitive and electrocatalytic properties. *J. Am. Chem. Soc.* **137**, 5590-5595 (2015).
33. Mefford JT, *et al.* Correlative operando microscopy of oxygen evolution electrocatalysts. *Nature* **593**, 67-73 (2021).
34. Bergmann A, *et al.* Unified structural motifs of the catalytically active state of Co(oxyhydr)oxides during the electrochemical oxygen evolution reaction. *Nat. Catal.* **1**, 711-719 (2018).
35. Heidary N, Kornienko N. Electrochemical biomass valorization on gold-metal oxide nanoscale heterojunctions enables investigation of both catalyst and reaction dynamics with operando surface-enhanced Raman spectroscopy. *Chem. Sci.* **11**, 1798-1806 (2020).
36. Sun S, *et al.* Shifting oxygen charge towards octahedral metal: a way to promote water oxidation on cobalt spinel oxides. *Angew. Chem. Int. Ed.* **58**, 6042-6047 (2019).
37. Cai Z, *et al.* Single-crystalline ultrathin Co₃O₄ nanosheets with massive vacancy defects for enhanced electrocatalysis. *Adv. Energy Mater.* **8**, 1701694 (2018).
38. Xiao Z, *et al.* Filling the oxygen vacancies in Co₃O₄ with phosphorus: an ultra-efficient electrocatalyst for overall water splitting. *Energy. Environ. Sci.* **10**, 2563-2569 (2017).
39. Amin HMA, Baltruschat H. How many surface atoms in Co₃O₄ take part in oxygen evolution? Isotope labeling together with differential electrochemical mass spectrometry. *Phys. Chem. Chem. Phys.*

19, 25527-25536 (2017).

40. Choi S, *et al.* Mechanistic investigation of biomass oxidation using nickel oxide nanoparticles in a CO₂-saturated electrolyte for paired electrolysis. *J. Phys. Chem. Lett.* **11**, 2941-2948 (2020).
41. Bredar ARC, Chown AL, Burton AR, Farnum BH. Electrochemical impedance spectroscopy of metal oxide electrodes for energy applications. *ACS Appl. Energy Mater.* **3**, 66-98 (2020).
42. Chen W, *et al.* Unveiling the Electrooxidation of urea: intramolecular coupling of the N-N Bond. *Angew. Chem. Int. Ed.* **60**, 7297-7307 (2021).
43. Wang HY, Hung SF, Chen HY, Chan TS, Chen HM, Liu B. In operando identification of geometrical-site-dependent water oxidation activity of spinel Co₃O₄. *J. Am. Chem. Soc.* **138**, 36-39 (2016).
44. Cha HG, Choi KS. Combined biomass valorization and hydrogen production in a photoelectrochemical cell. *Nat. Chem.* **7**, 328-333 (2015).
45. Lu Y, *et al.* Hierarchically nanostructured NiO-Co₃O₄ with rich interface defects for the electro-oxidation of 5-hydroxymethylfurfural. *Sci. China Chem.* **63**, 980-986 (2020).
46. Blochl PE. Projector augmented-wave method. *Phys. Rev. B Condens. Matter* **50**, 17953-17979 (1994).
47. Kresse G, Hafner J. Ab initio molecular dynamics for liquid metals. *Phys. Rev. B Condens. Matter* **47**, 558-561 (1993).
48. Kresse G, Joubert D. From ultrasoft pseudopotentials to the projector augmented-wave method. *Matter Mater. Phys.* **59**, 1758-1775 (1999).
49. Perdew JP, Burke K, Ernzerhof M. Generalized gradient approximation made simple. *Phys. Rev. Lett.* **77**, 3865-3868 (1996).
50. Grimme S. Semiempirical GGA-type density functional constructed with a long-range dispersion correction. *J. Comput. Chem.* **27**, 1787-1799 (2006).
51. Mills G, Jonsson H. Quantum and thermal effects in H₂ dissociative adsorption: Evaluation of free energy barriers in multidimensional quantum systems. *Phys. Rev. Lett.* **72**, 1124-1127 (1994).

Figures

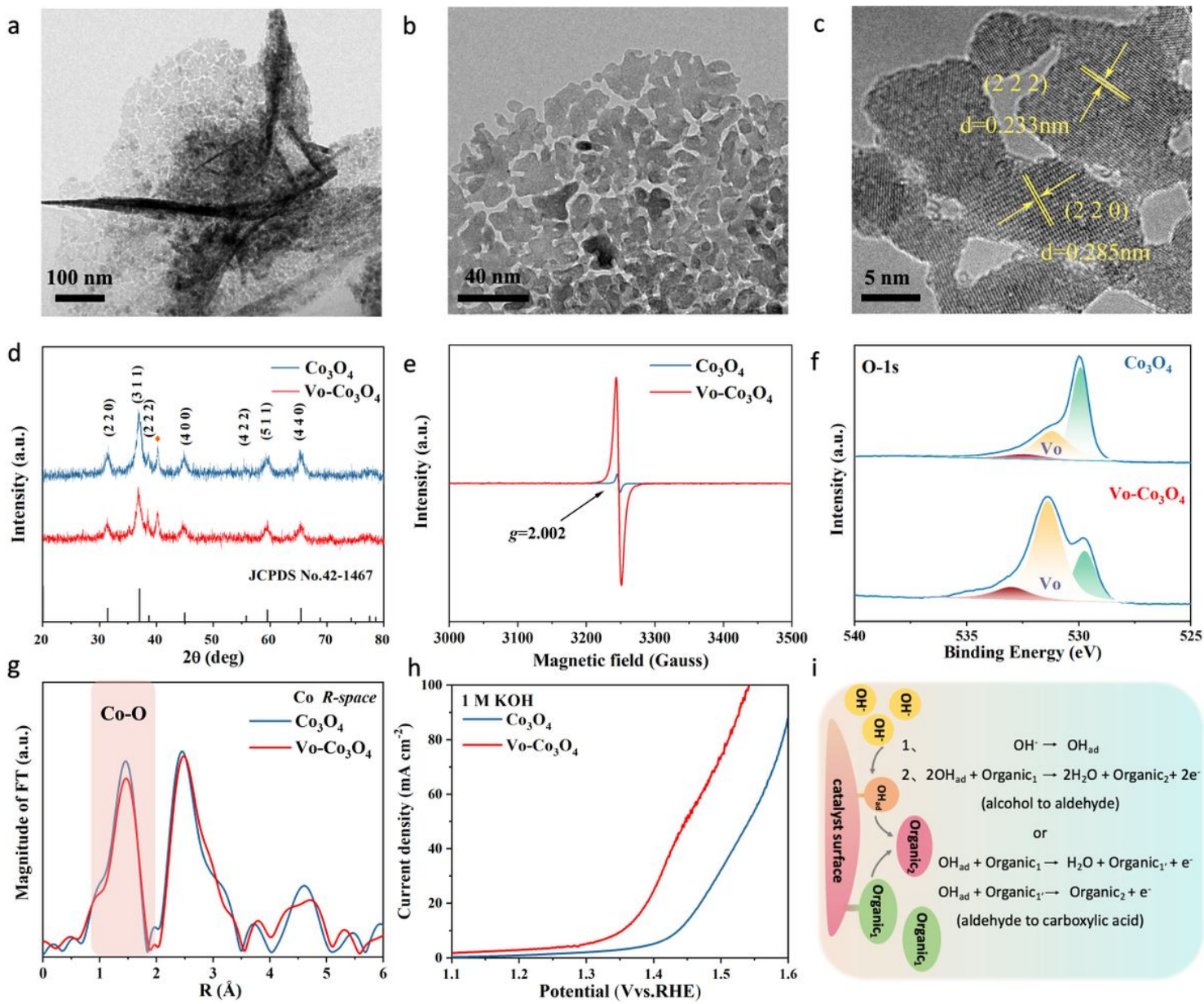


Figure 1

Materials and electrochemical activity characterization of Co_3O_4 and $\text{Vo-Co}_3\text{O}_4$. a-b TEM and c HR-TEM images of $\text{Vo-Co}_3\text{O}_4$. d XRD patterns of Co_3O_4 and $\text{Vo-Co}_3\text{O}_4$; e EPR spectra of Co_3O_4 and $\text{Vo-Co}_3\text{O}_4$; g O 1s XPS spectra fitting for Co_3O_4 and $\text{Vo-Co}_3\text{O}_4$. f EXAFS spectra of Co_3O_4 and $\text{Vo-Co}_3\text{O}_4$; h LSV curves of $\text{Vo-Co}_3\text{O}_4$ and Co_3O_4 in 1 M KOH at a scan rate of 5 mV s⁻¹; i the scheme for the process of HMFOR.

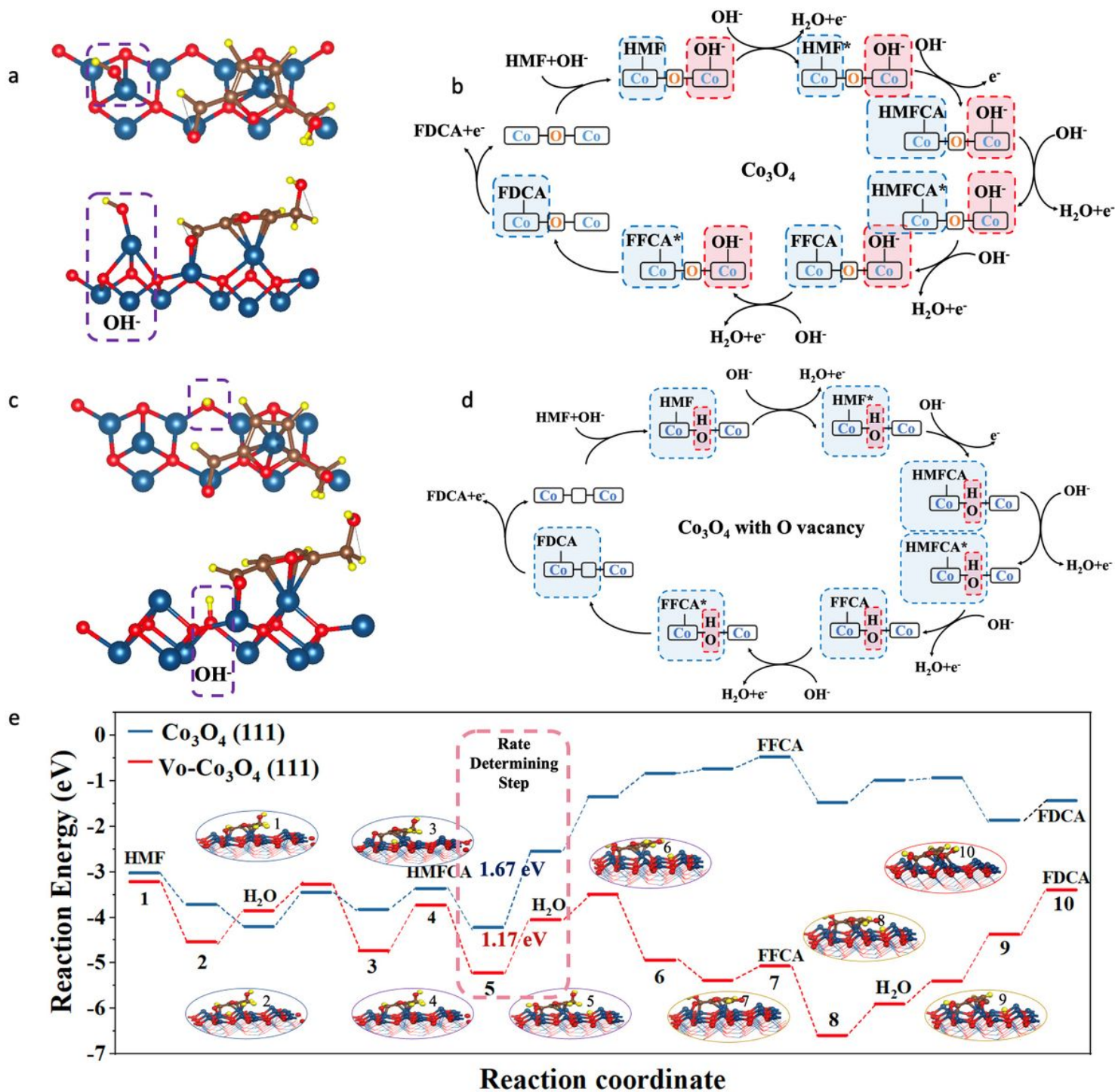


Figure 2

Theoretical study for HMFOR process. a The scheme for adsorption model on Co_3O_4 , in which HMF molecule was adsorbed on the octahedral and tetrahedral sites, and OH^- was adsorbed on the nearby octahedral sites. b The reaction mechanism of HMFOR on Co_3O_4 . c The scheme for adsorption model on $\text{Vo-Co}_3\text{O}_4$, in which OH^- was filled into Vo , and HMF molecule was adsorbed on the octahedral and tetrahedral sites. d The reaction mechanism of HMFOR on $\text{Vo-Co}_3\text{O}_4$. e Free energies of HMFOR step via path I on $\text{Vo-Co}_3\text{O}_4$ and Co_3O_4 .

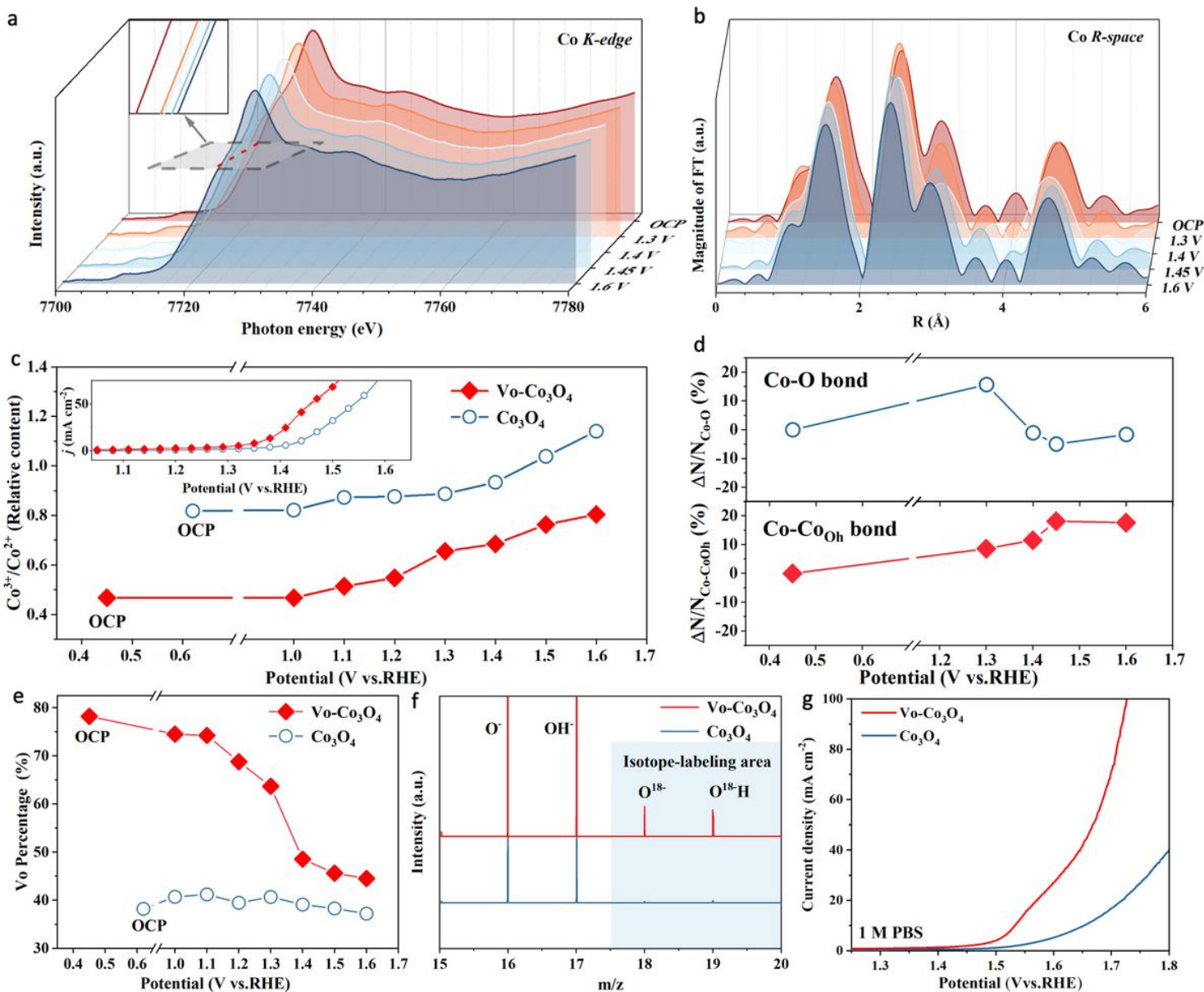


Figure 3

Operando physical and electrochemical characterization for identifying the role of oxygen vacancies. a The operando XANES spectra of Vo-Co₃O₄. b The EXAFS spectra of Vo-Co₃O₄. c The relative ratio of Co³⁺/Co²⁺ for Vo-Co₃O₄ and Co₃O₄ in nearside, the photon energy of Co pre-edge in starboard. Inset is the LSV curves of Vo-Co₃O₄ and Co₃O₄ in 1 M KOH with 50 mM HMF; d Structural coherence changes in EXAFS coordination number of Co-O bond and Co^{OH}-Co^{OH} bond under applied potential relative with the OCP state; e the relative content of Vo on Vo-Co₃O₄ and Co₃O₄ based on quasi-operando O 1s spectra. f TOF-SIMS spectra of Vo-Co₃O₄ and Co₃O₄ after HMFOR. g The LSV curves of Vo-Co₃O₄ and Co₃O₄ in 1 M PBS with 50 mM HMF.

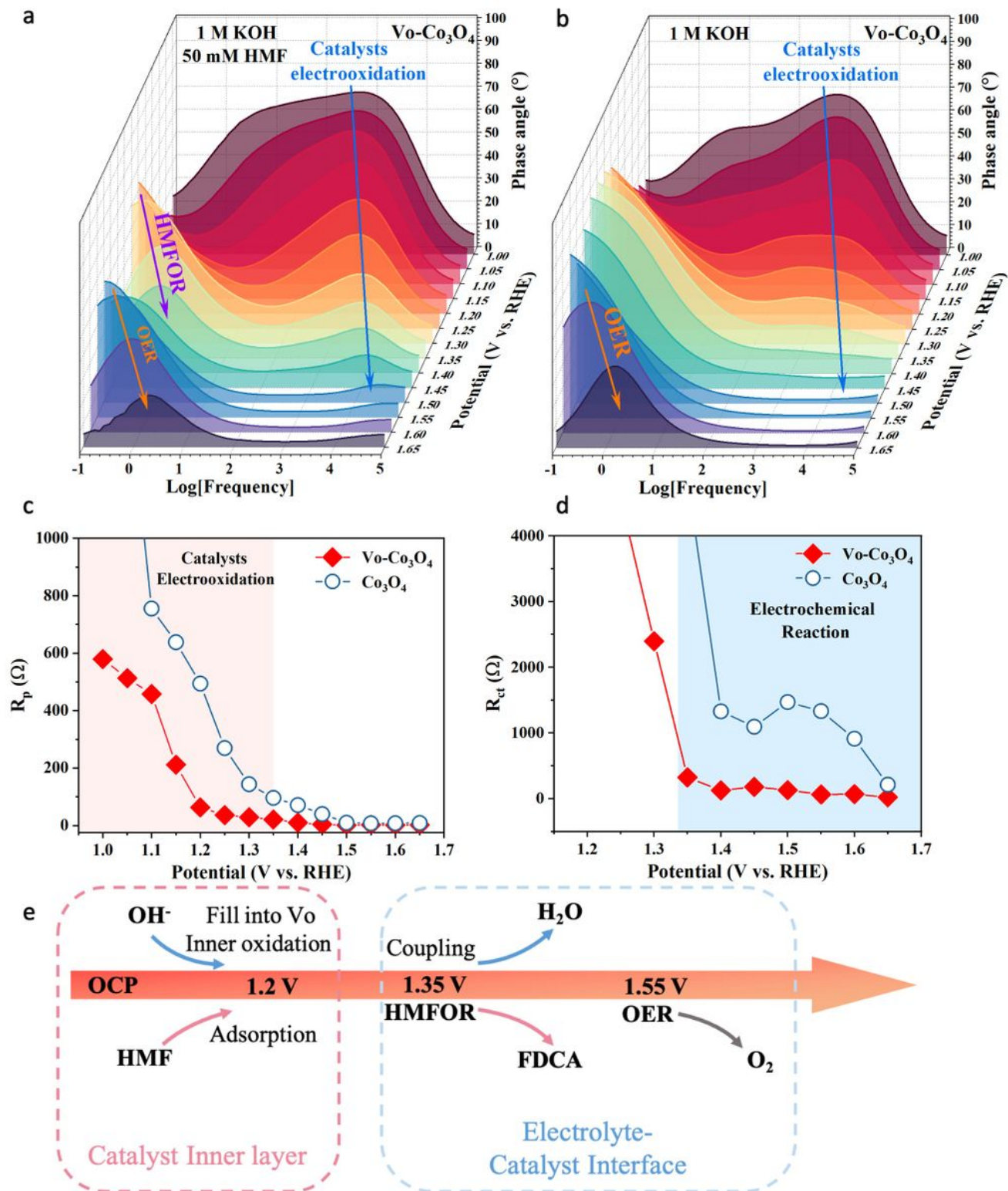


Figure 4

EIS study for the exploration of the relationship between electrode materials and interfacial reaction. a-b Bode phase plots of the in-situ EIS on Vo-Co₃O₄ in a 1 M KOH with 50 mM HMF, and b 1 M KOH; c The resistance of the electrode inner oxidation (R_p) on Vo-Co₃O₄ and Co₃O₄. d The resistance of the electrode interface reaction (R_{ct}) on Vo-Co₃O₄ and Co₃O₄. e The scheme of fit model and the relationship between structure-activity-potential.

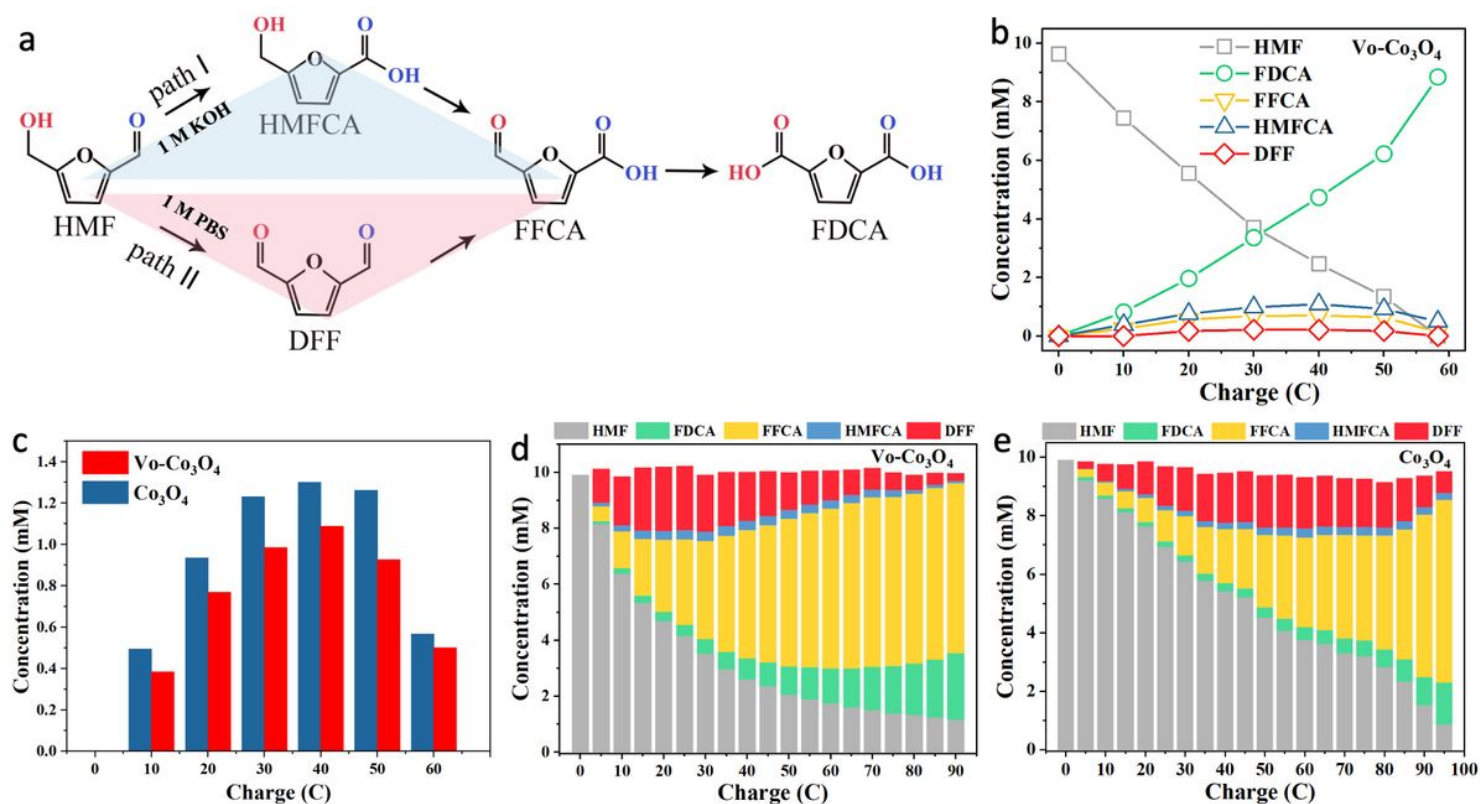


Figure 5

Investigation of the reaction pathway and reaction process of HMFOR. a Two possible reaction pathways for HMF oxidation. b The concentration of substrates, intermediates, and products during HMFOR for Vo-Co₃O₄. c The concentration of HMFCFA during HMFOR for Vo-Co₃O₄ and Co₃O₄ in 1 M KOH. d-e The concentration of substrates, intermediates and products during HMFOR for Vo-Co₃O₄ (d) and Co₃O₄ (e) in 1 M PBS, respectively.

Supplementary Files

This is a list of supplementary files associated with this preprint. Click to download.

- [SIVoCo3O4forHMFOR20210608.docx](#)